# Efficient Water Oxidation Using Nanostructured α-Nickel-Hydroxide as an Electrocatalyst

Minrui Gao, Wenchao Sheng, Zhongbin Zhuang, Qianrong Fang, Shuang Gu, Jun Jiang, and Yushan Yan*

Department of Chemical and Biomolecular Engineering, Center for Catalytic Science and Technology, University of Delaware, Newark, Delaware 19716, United States

Ⓢ Supporting Information

**ABSTRACT:** Electrochemical water splitting is a clean technology that can store the intermittent renewable wind and solar energy in $H_2$ fuels. However, large-scale $H_2$ production is greatly hindered by the sluggish oxygen evolution reaction (OER) kinetics at the anode of a water electrolyzer. Although many OER electrocatalysts have been developed to negotiate this difficult reaction, substantial progresses in the design of cheap, robust, and efficient catalysts are still required and have been considered a huge challenge. Herein, we report the simple synthesis and use of α-$Ni(OH)_2$ nanocrystals as a remarkably active and stable OER catalyst in alkaline media. We found the highly nanostructured α-$Ni(OH)_2$ catalyst afforded a current density of 10 mA cm$^{-2}$ at a small overpotential of a mere 0.331 V and a small Tafel slope of ~42 mV/decade, comparing favorably with the state-of-the-art $RuO_2$ catalyst. This α-$Ni(OH)_2$ catalyst also presents outstanding durability under harsh OER cycling conditions, and its stability is much better than that of $RuO_2$. Additionally, by comparing the performance of α-$Ni(OH)_2$ with two kinds of β-$Ni(OH)_2$, all synthesized in the same system, we experimentally demonstrate that α-$Ni(OH)_2$ effects more efficient OER catalysis. These results suggest the possibility for the development of effective and robust OER electrocatalysts by using cheap and easily prepared α-$Ni(OH)_2$ to replace the expensive commercial catalysts such as $RuO_2$ or $IrO_2$.
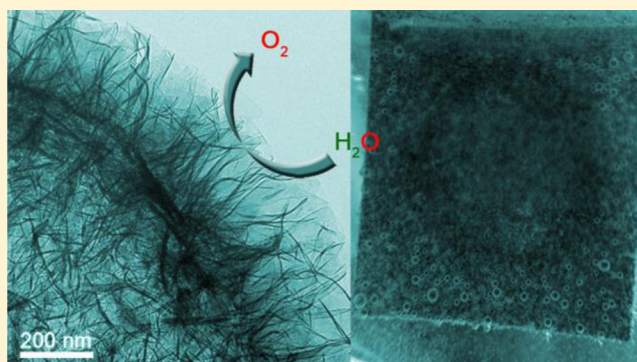
## INTRODUCTION

Electrochemical water splitting ($2H_2O \rightarrow 2H_2 + O_2$) provides an attractive path to produce hydrogen ($H_2$) fuels and to store the electricity from renewable but intermittent sources (e.g., wind and sunlight).[1−3] However, large-scale electrochemical water splitting is greatly hindered by the sluggish anodic oxygen evolution reaction (OER) where O−H bond breaking and attendant O−O bond formation are necessary.[1,4−6] An appropriate OER catalyst can help to address this challenge by efficiently coupling multiple proton and electron transfers for evolving $O_2$ under low overpotentials ($\eta$).[4,5,7] Currently, the most widely used and most efficient OER catalysts are the expensive and scarce ruthenium (Ru) and iridium (Ir) oxides.[8,9] A great many alternative OER catalysts based on abundant 3d metals (Fe, Co, Ni, Mn), including simple[10−19] and mixed-metal oxides (hydroxides),[20−25] chalcogenides,[26,27] phosphates,[28,29] borides,[30] perovskites,[4,31,32] and molecular catalysts,[33,34] have been studied, but substantial progress is still needed in reducing the cost and improving activity and stability of the OER catalysts.

Among the 3d metal-based OER catalysts, Ni-containing materials have garnered special attention because of their earth-abundant nature (Ni is the ninth most abundant element in the Earth's crust) and their good water oxidation potential.[35] High OER activity has been achieved with, for instance, Ni oxides,[16−19] Ni-containing mixed-metal oxides (hydroxides),[16,19,20,23] and various Ni-containing perovskites.[4,31,32] Very recently, Ni film deposited on n-type silicon was used as an effective OER electrocatalyst for photoelectrochemical water oxidation in both aqueous 1 M KOH (pH ~14) and aqueous borate buffer (pH ~9.5).[36] Surprisingly, $Ni(OH)_2$, a widely used positive electrode material in alkaline batteries, has not received adequate attention in the field of water oxidation,[37] likely due to the fact that parasitic OER is undesirable and has to be suppressed during the battery cathode charging process.[38,39] Recently, Markovic et al. studied different 3d-metal hydr(oxy)oxides modified platinum (Pt) single crystals and determined the highest activities of $Ni^{2+\sigma}O^{\sigma}(OH)_{2-\sigma}$/Pt(111) ($0 \leq \sigma \leq 1.5$, $\sigma = 0$ in the hydrogen evolution reaction (HER) region and $\sigma = 1$ in the OER region) for both HER and OER ascribing to optimum $OH_{ad}^{-}$–$Ni^{2+\sigma}$ bond strength.[40,41] Nocera et al. provided evidence for the formation of active Ni hydroxides in electrodeposited Ni-borate thin films.[42] On the basis of in situ X-ray absorption near-edge structure spectroscopy studies, the same group further pointed out that the γ-NiOOH phase is needed for high OER activity.[42,43]
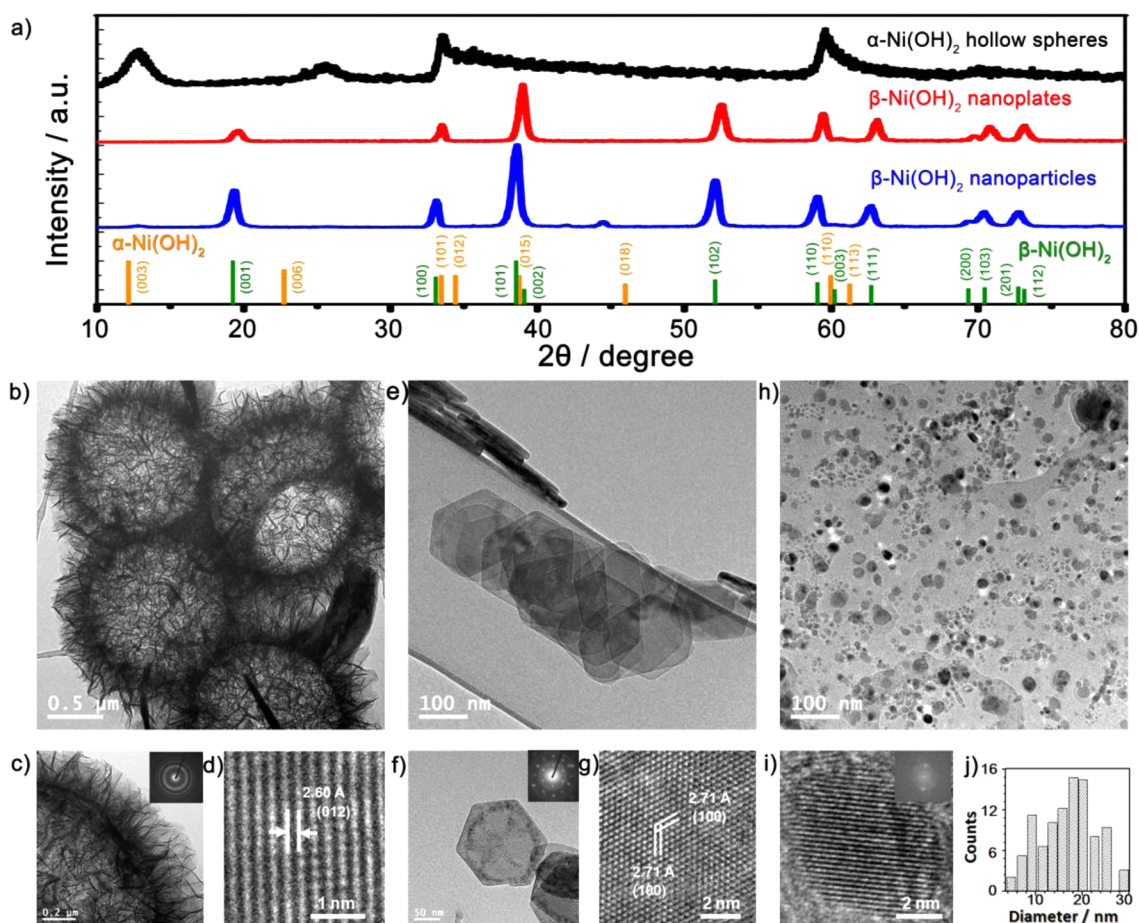
**Figure 1.** (a) XRD patterns for as-prepared $\alpha$-Ni(OH)$_2$ hollow spheres, $\beta$-Ni(OH)$_2$ nanoplates, and $\beta$-Ni(OH)$_2$ nanoparticles. (b–d) TEM, enlarged TEM, and HRTEM images for $\alpha$-Ni(OH)$_2$ hollow spheres, respectively. Inset in panel c shows the corresponding SAED pattern. (e–g) TEM, enlarged TEM, and HRTEM images for $\beta$-Ni(OH)$_2$ nanoplates, respectively. Inset in panel f shows the corresponding SAED pattern. (h–j) TEM, HRTEM images, and particle-size histogram for $\beta$-Ni(OH)$_2$ nanoparticles, respectively. Inset in panel i shows the corresponding FFT pattern.

Herein, we show that $\alpha$-Ni(OH)$_2$ nanocrystals are a highly active and stable OER catalyst with performance superior to that of ruthenium oxide (RuO$_2$) in alkaline electrolyte, and the fabrication of $\alpha$-Ni(OH)$_2$ is simple, economic, and easily scaled up. Additionally, by comparing the performance of $\alpha$-Ni(OH)$_2$ with two kinds of $\beta$-Ni(OH)$_2$, we experimentally demonstrate that $\alpha$-Ni(OH)$_2$ effects more efficient OER catalysis. These results strongly suggest the promise of an efficient, robust, and economic OER electrocatalyst based on $\alpha$-Ni(OH)$_2$.

### ■ EXPERIMENTAL SECTION

**Chemicals.** All chemical reagents were used as received without further purification.

**Synthesis of Nanosheet-Assembled $\alpha$-Ni(OH)$_2$ Hollow Spheres.** In a typical procedure, 1 mmol (0.291g) of Ni(NO$_3$)$_2$·6H$_2$O was added into 20 mL of ethanol in a beaker under magnetic stirring. After about 5 min of stirring, 2 mL of oleylamine and 10 mL of ethanol were quickly added, and the stirring was continued for 0.5 h to produce a homogeneous solution, which was then transferred into a 50-mL Teflon-lined autoclave. The autoclave was sealed and maintained at 180 °C for 15 h in a convection oven and then naturally cooled to room temperature. The resulting green sample was collected and washed with cyclohexane, distilled water, and ethanol to remove organics, ions, and possible remnants and dried under vacuum at 60 °C for 6 h.

**Synthesis of $\beta$-Ni(OH)$_2$ Hexagonal Nanoplates.** To prepare $\beta$-Ni(OH)$_2$ hexagonal nanoplates, the same synthesis procedure for $\alpha$-

Ni(OH)$_2$ hollow spheres was used except that the 20 mL of ethanol was replaced by 20 mL of distilled water.

**Synthesis of $\beta$-Ni(OH)$_2$ Nanoparticles.** To prepare $\beta$-Ni(OH)$_2$ nanoparticles, the same synthesis procedure for $\alpha$-Ni(OH)$_2$ hollow spheres was used except that the 20 mL of ethanol was replaced by 20 mL of acetone.

**Materials Characterization.** The as-synthesized samples were examined by X-ray powder diffraction (XRD), which was carried out on a Philips X'Pert powder diffractometer with Cu K$\alpha$ radiation ($\lambda = 1.5418$ Å). The particle size and morphology of the as-synthesized samples were determined by using a JEM 2000FX transmission electron microscope (TEM). The HRTEM observation and selected-area electron diffraction (SAED) were carried out on a high-resolution transmission electron microscope (JEM-2010F) with an acceleration voltage of 200 kV. All samples were prepared by dropping the ethanol suspension containing uniformly dispersed nanocrystals onto the carbon-coated copper grids. Scanning electron microscope (SEM) images were recorded on a JEOL JSM 7400 microscope with a field-emission gun capable of 1.5 nm resolution. Adsorption isotherms were collected on a Micromeritics ASAP 2010 at 77 K using N$_2$ as the adsorbate gas. The surface areas were evaluated using the Brunauer–Emmett–Teller (BET) equation in the $P/P_0$ range of 0.05–0.4. Before the measurements, all samples were degassed at 383 K under vacuum for 2 h.

**Electrocatalytic Study.** Electrochemical measurements were performed at room temperature using a rotating disk working electrode made of glassy carbon (PINE, 5 mm diameter, 0.196 cm$^2$) connected to a multichannel potentiostat (VMP2, Princeton Applied Research). The glassy carbon electrode was polished to a mirror finish
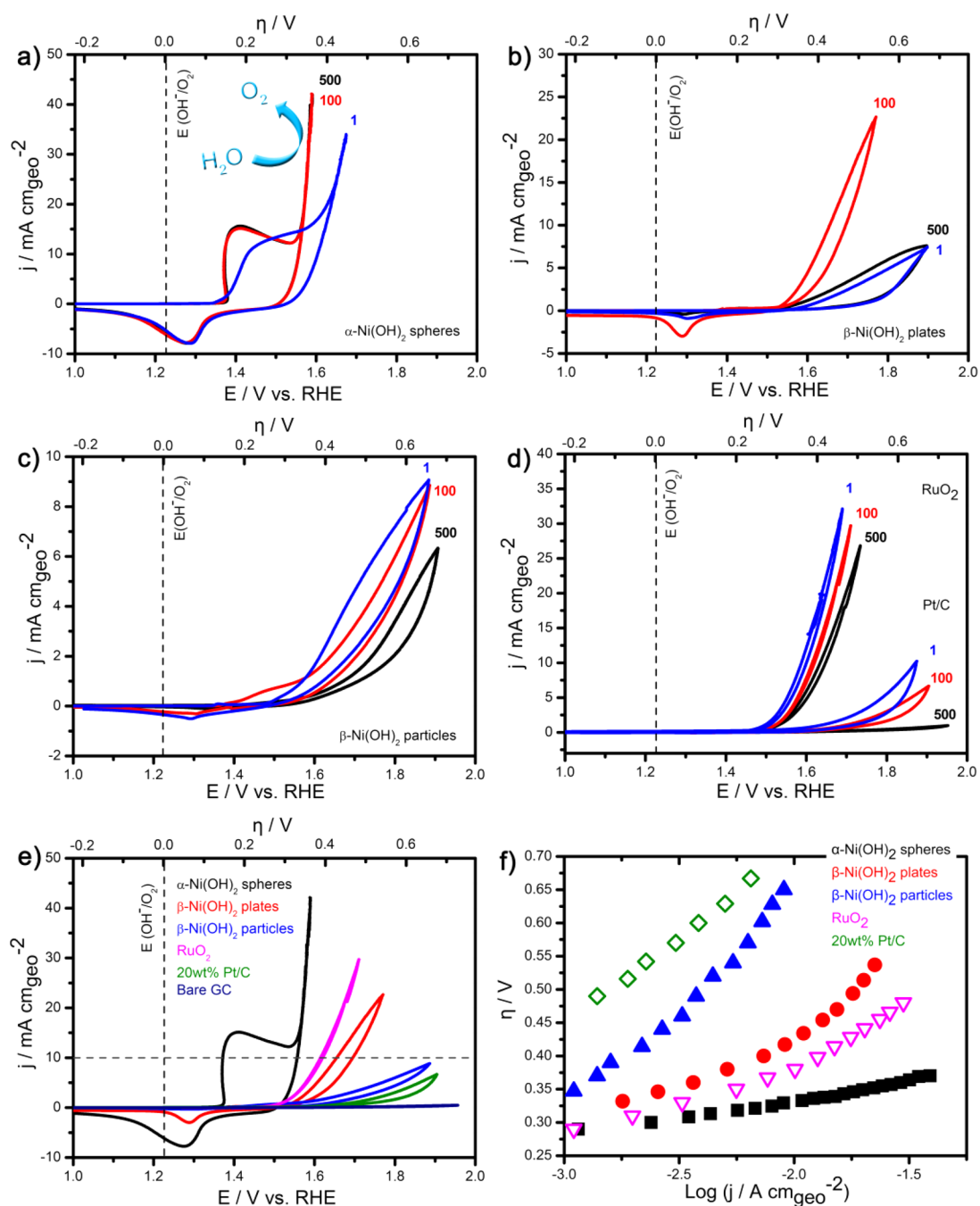
**Figure 2.** (a−d) CV curves recorded at 1st cycle, 100th cycle, and 500th cycle for $\alpha$-Ni(OH)$_2$ hollow spheres (a), $\beta$-Ni(OH)$_2$ nanoplates (b), $\beta$-Ni(OH)$_2$ nanoparticles (c), and commercial RuO$_2$ as well as 20 wt % Pt/C catalysts (d), respectively. (e) Comparison of CVs recorded at 100th cycle for bare GC electrode and modified GC electrodes comprising the $\alpha$- and $\beta$-Ni(OH)$_2$ nanocrystals, RuO$_2$, and 20 wt % Pt/C. (f) Tafel plots ($\eta$ vs log current) of OER currents derived from (e) using the anodic sweep (for $\alpha$-Ni(OH)$_2$ catalyst; however, cathodic sweep was used to avoid the interference of $\alpha$-Ni(OH)$_2$ oxidation peak). All measurements were performed in O$_2$-purged 0.1 M KOH (pH ~13). All CV curves were recorded at a sweep rate of 10 mV s$^{-1}$ after given number of cycles between 0.06 and 1.96 V vs RHE at a sweep rate of 250 mV s$^{-1}$. CV curves were iR-compensated. Catalyst loading was ~0.2 mg cm$^{-2}$.

and thoroughly cleaned before use. Pt coil and Ag/AgCl (PINE, 4 M KCl) were used as counter and reference electrodes, respectively. The potentials reported in our work were referenced to the reversible hydrogen electrode (RHE) through RHE calibration,[12] and in 0.1 M KOH, $E$(RHE) = $E$(Ag/AgCl) + 0.96 V.

The preparation method of the working electrodes is as follows. In brief, 5 mg of catalyst powder was dispersed in 1 mL of 3:1 v/v water/isopropyl alcohol mixed solvent with 45 $\mu$L of Nafion solution (5 wt %, Sigma-Aldrich). The mixture was then ultrasonicated for about 0.5 h to generate a homogeneous ink. Next, 8 $\mu$L of the dispersion was

transferred onto the glassy carbon disk, leading to a catalyst loading of ~0.2 mg cm$^{-2}$. Finally, the as-prepared catalyst film was dried at room temperature. For comparison, a bare glassy carbon electrode that had been polished and cleaned was also dried for electrochemical measurement.

Before the electrochemical measurement, the electrolyte (0.1 M KOH, 99.99% metal purity, pH ~13) was purged by O$_2$ (ultra-high-grade purity, PRAXAIR) for at least 0.5 h to ensure the saturation of the electrolyte. The cyclic voltammetry (CV) curves were obtained by sweeping the potential from 0.96 to 1.96 V vs RHE at room

temperature and 1600 rpm, with a sweep rate of 10 mV s$^{-1}$. The impedance measurements were performed in the same configuration at open circuit potential over a frequency range from 20 kHz to 1 mHz at the amplitude of the sinusoidal voltage of 5 mV and room temperature. For the stability evaluations, the potential of the electrodes cycled between a wide potential range of 0.06−1.96 V vs RHE at a sweep rate of 250 mV s$^{-1}$. At the end of the cycling experiment, CV curves were obtained with a sweep rate of 10 mV s$^{-1}$. Chronoamperometry data were collected for $\alpha$-Ni(OH)$_2$ and RuO$_2$ coated carbon fiber papers (1 cm$^2$, catalyst loading 5 mg) at a $\eta$ of 0.35 V.

**Calculation Method.** Details concerning the calculation of mass activity, specific activity, and turnover frequency (TOF) are shown below.

The values of mass activity (A g$^{-1}$) were calculated from the catalyst loading $m$ (0.2 mg cm$_{geo}$$^{-2}$) and the measured current density $j$ (mA cm$_{geo}$$^{-2}$) at $\eta$ = 0.35 V:

$$\text{mass activity} = \frac{j}{m} \tag{1}$$

The values of specific activity (mA cm$^{-2}$) were calculated from the BET surface area $S_{BET}$ (m$^2$ g$^{-1}$), catalyst loading $m$ (0.2 mg cm$_{geo}$$^{-2}$), and the measured current density $j$ (mA cm$_{geo}$$^{-2}$) at $\eta$ = 0.35 V:

$$\text{specific activity} = \frac{j}{10 \cdot S_{BET} \cdot m} \tag{2}$$

The values of TOF were calculated by assuming that every metal atom is involved in the catalysis (lower TOF limits were calculated):

$$\text{TOF} = \frac{j \cdot S_{geo}}{4F \cdot n} \tag{3}$$

Here, $j$ (mA cm$_{geo}$$^{-2}$) is the measured current density at $\eta$ = 0.35 V, $S_{geo}$ (0.196 cm$^2$) is the surface area of glassy carbon disk, the number 4 means 4 electrons per mole of O$_2$, $F$ is Faraday's constant (96485.3 C mol$^{-1}$), and $n$ is the moles of the metal atom on the electrode calculated from $m$ and the molecular weight of the coated catalysts.

## ■ RESULTS AND DISCUSSION

Phase-controllable $\alpha$-Ni(OH)$_2$ and $\beta$-Ni(OH)$_2$ were successfully synthesized in a simple solvothermal system (Supplementary Figure S1). X-ray diffraction (XRD) patterns (Figure 1a) support the formation of pure hexagonal $\alpha$-Ni(OH)$_2$ (JCPDS 380715) and hexagonal $\beta$-Ni(OH)$_2$ (JCPDS 140117) phases, respectively. Of note, the positively shifted diffraction angles of the $\alpha$-Ni(OH)$_2$ (003) and (006) planes suggest a decrease in the $d$ spacing along the $c$-axis, presumably due to the extent and type of the intercalated anions in the Ni(OH)$_2$ lattice.[44] Similar positive shifts were also reported for sonochemically synthesized $\alpha$-Ni(OH)$_2$,[45] precipitation-induced $\alpha$-Ni(OH)$_2$ particles,[46] and microwave-stimulated $\alpha$-Ni(OH)$_2$ flakes.[47] The asymmetric nature of the reflection at $2\theta$ = 33.6° indicates the formation of turbostratic $\alpha$-Ni(OH)$_2$ phase.[45,46] Typical structural and morphological analyses of the obtained samples are provided in Figure 1b−j (also Supplementary Figure S2). Transmission electron microscopy (TEM) images in Figure 1b,c show that the $\alpha$-Ni(OH)$_2$ hollow spheres with a diameter of ~1.8 $\mu$m are actually constructed by numerous ultrathin nanosheets (see Supplementary Figure S3 for proposed formation mechanism). Selected-area electron diffraction (SAED) pattern taken from a single hollow sphere shows the polycrystalline nature owing to the nanosheets-assembled microstructure (inset in Figure 1c). High-resolution TEM (HRTEM) image of a selected nanosheet shows lattice fringes of $\alpha$-Ni(OH)$_2$ (012) planes with a $d$ spacing of 2.60 Å (Figure 1d). When the ethanol solvent used in $\alpha$-Ni(OH)$_2$

synthesis was replaced by water, nearly uniform hexagonal $\beta$-Ni(OH)$_2$ nanoplates with an edge length of ~86 nm were obtained (Figure 1e,f). The SAED pattern shows perfect rhombus diffraction spots, indicating the single-crystalline nature of $\beta$-Ni(OH)$_2$ nanoplates (inset in Figure 1f). The HRTEM image taken near the nanoplate center reveals distinct lattice fringes with $d$ spacing of 2.71 Å, corresponding to the (100) lattice planes of $\beta$-Ni(OH)$_2$ (Figure 1g). When the solvent was switched to acetone, $\beta$-Ni(OH)$_2$ nanoparticles (Figure 1h) with average size of ~16 nm (Figure 1j) were harvested. The HRTEM image and corresponding fast Fourier transform (FFT) (Figure 1i and inset) reveal that the highly crystalline nanoparticle shows a $d$ spacing of 2.30 Å, corresponding to the (002) planes of the hexagonal $\beta$-Ni(OH)$_2$ phase.

$\alpha$- and $\beta$-Ni(OH)$_2$ can be easily oxidized to $\gamma$- and $\beta$-NiOOH,[48] respectively (Supplementary Figure S4) and are used here as model systems to examine which of the two phases, $\gamma$-NiOOH and $\beta$-NiOOH, is the more active OER phase. The successful fabrication of $\alpha$- and $\beta$-Ni(OH)$_2$ in a similar reaction system makes this assessment highly preferable to avoid other effects such as different reaction temperatures and times as well as different surfactants used in the synthesis. To this end, $\alpha$- and $\beta$-Ni(OH)$_2$ thin films were prepared onto glassy carbon (GC) electrodes for cyclic voltammetry (CV) in O$_2$-saturated 0.1 M KOH. The ohmic potential drop ($iR$) losses from the solution resistance were corrected (Supplementary Figure S5). Figure 2a shows CVs of $\alpha$-Ni(OH)$_2$ hollow spheres obtained after different numbers of cycles. The quasi reversible oxidation and reduction peaks ascribed to the oxidation of $\alpha$-Ni(OH)$_2$ to $\gamma$-NiOOH and the successive reduction back to $\alpha$-Ni(OH)$_2$ can be observed in the first CV cycle.[48,49] A second oxidation wave with an onset potential of ~1.63 V attributed to catalytic water oxidation is also observed (see Supplementary Movie S1 for O$_2$ evolution experiment). With further cycling, the above oxidation/reduction waves increased in amplitude and approached a stable value after 100 cycles (Figure 2a and Supplementary Figure S6a), suggesting the activation of $\alpha$-Ni(OH)$_2$ and the increase of the electroactive species (i.e., $\gamma$-NiOOH) on the electrode surface,[48,49] which is in line with the negatively shifted OER catalytic wave with a smaller onset potential of ~1.54 V (Figure 2a). Of note, the electrochemical features of $\alpha$-Ni(OH)$_2$ hollow spheres became stable after 100 cycles, and no deactivation was observed during the following CV cycles, even up to 500 cycles (Figure 2a and Supplementary Figure S6a). Figure 2b and c shows that the redox waves assignable to the $\beta$-Ni(OH)$_2$/$\beta$-NiOOH redox couple are all ill-shaped. The OER catalytic current of $\beta$-Ni(OH)$_2$ nanoplates (Figure 2b and Supplementary Figure S6b) increases initially until reaching a maximum after 100 cycles and then drops quickly, indicative of poor catalyst stability. For $\beta$-Ni(OH)$_2$ nanoparticles (Figure 2c), the OER current decreases slightly during the first 100 cycles and then drops quickly during the following 400 cycles. For comparison, similar measurements for both commercial RuO$_2$ (Sigma-Aldrich) and Pt/C catalysts (ElectroChem. Inc., 20 wt %) were performed. As expected, RuO$_2$ catalyst displays an excellent OER performance with an onset potential of ~1.48 V in the first cycle (Figure 2d), in line with the previous value for RuO$_2$ in 0.1 M KOH.[9] However, this OER activity gradually but continuously decreases with CV cycling (Figure 2d, Supplementary Figures S6c and S7), consistent with previous reports that RuO$_2$ and IrO$_2$ suffer from large chemical degradation during OER process.[35] Figure

## Table 1. Comparison of OER Activity Data for Different Catalysts[a]

| catalyst | $\eta$ at $J = 10$ mA cm$^{-2}$ (mV)[b] | mass activity at $\eta = 0.35$ V (A g$^{-1}$) | specific activity at $\eta = 0.35$ V (mA cm$^{-2}$)[c] | Tafel slope (mV dec$^{-1}$) | TOF at $\eta = 0.35$ V (s$^{-1}$)[d] |
|---|---|---|---|---|---|
| $\alpha$-Ni(OH)$_2$ spheres | 331 | 150.1 | 0.26 | 42 | 0.0361 |
| $\beta$-Ni(OH)$_2$ plates | 444 | 12.5 | 0.03 | 111 | 0.0030 |
| $\beta$-Ni(OH)$_2$ particles | | 4.7 | 0.01 | 246 | 0.0012 |
| RuO$_2$ | 387 | 30.2 | 0.23 | 90 | 0.0104 |
| 20 wt % Pt/C | | 10.5 | | 274 | 0.0053 |

[a]All data reflect the catalytic activity after potential sweeps for 100 cycles between −0.9 and 1 V vs Ag/AgCl. [b]The overpotential at 10 mA cm$^{-2}$ for $\alpha$-Ni(OH)$_2$ spheres was determined using the cathodic sweep of the corresponding CV curve shown in Figure 2e to avoid the interference of the $\alpha$-Ni(OH)$_2$ oxidation peak. [c]Specific activity is normalized to the BET surface area (see Supplementary Figure S8). [d]See Experimental Section for the calculation method.
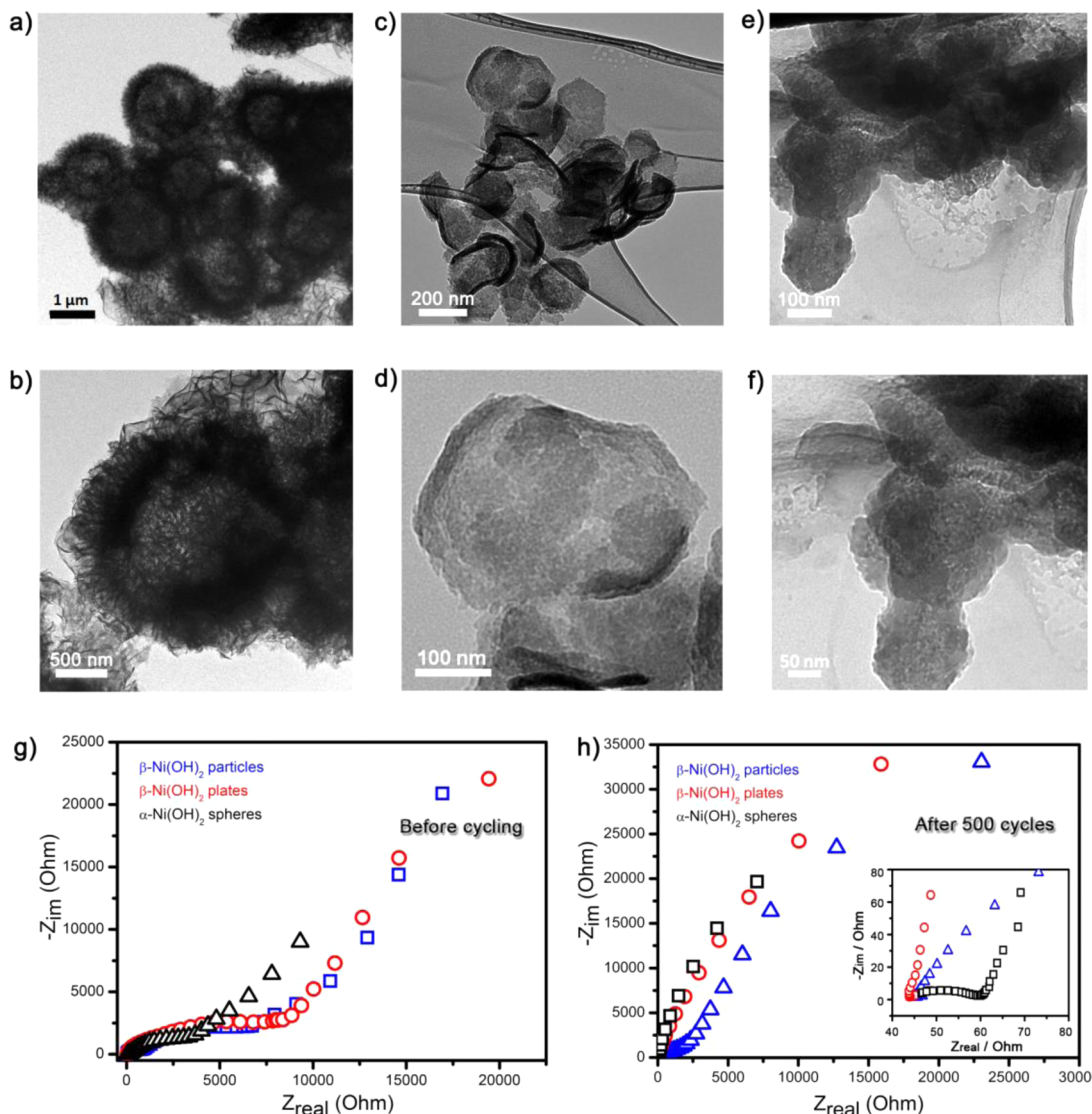


**Figure 3.** (a−f) TEM and HRTEM images taken after 500 cycles for $\alpha$-Ni(OH)$_2$ hollow spheres (a,b), $\beta$-Ni(OH)$_2$ nanoplates (c,d), and $\beta$-Ni(OH)$_2$ nanoparticles (e,f). (g,h) EIS Nyquist plots of the $\alpha$- and $\beta$-Ni(OH)$_2$ nanocrystals before (g) and after (h) 500 cycles. Inset in panel h shows corresponding Nyquist plot at the high-frequency range.

2d also shows that commercial Pt/C, a classical catalyst for the oxygen reduction reaction (ORR), bears only low OER activity, which degrades quickly with continued CV cycling (Supplementary Figure S6d).

Considering that severe degradation occurred at higher numbers of CV cycles (e.g., 500) for all OER catalysts except $\alpha$-Ni(OH)$_2$, we chose the OER data after 100 CV cycles for

comparison. As shown in Figure 2e, $\alpha$-Ni(OH)$_2$ hollow spheres afford the largest oxygen-evolving current among the studied catalysts. Remarkably, the current density of 10 mA cm$^{-2}$, which is a metric relevant to solar fuel synthesis,[11] can be achieved at $\eta$ (iR-corrected) of ∼0.33 V for the $\alpha$-Ni(OH)$_2$ catalyst, smaller than that of $\beta$-Ni(OH)$_2$ plates (∼0.44 V) and RuO$_2$ (∼0.39 V) catalysts (Figure 2e and Table 1). By contrast,
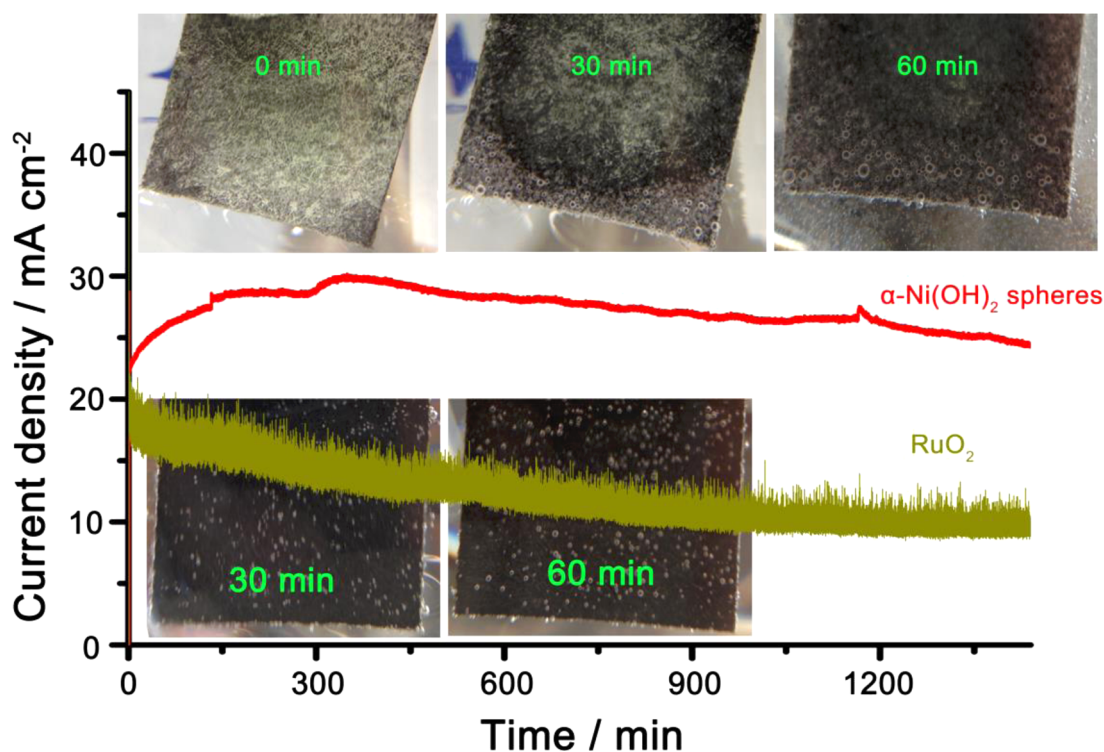
**Figure 4.** Chronoamperometry data ($j$–$t$) recorded on $\alpha$-Ni(OH)$_2$ hollow spheres and commercial RuO$_2$ catalyst at a constant $\eta$ of 0.35 V measured in 0.1 M KOH. The catalyst loading on CFP was 5 mg cm$^{-2}$ based on the geometric CFP area. Inset digital photos show the O$_2$ bubbles on $\alpha$-Ni(OH)$_2$-modified CFP (top) and RuO$_2$-modified CFP (bottom) at different time points.

$\beta$-Ni(OH)$_2$ nanoparticles and commercial Pt/C fail to reach such current density. The OER kinetics of the above catalysts is also estimated by corresponding Tafel plots (log $j$–$\eta$). The Tafel slope of $\alpha$-Ni(OH)$_2$ hollow spheres is a mere ~42 mV dec$^{-1}$, which is much smaller than that of all other catalysts studied including RuO$_2$ (Figure 2f and Table 1), demonstrating its more efficient kinetics of water oxidation. Note here that the Tafel slope of the $\alpha$-Ni(OH)$_2$ catalyst is comparable to or smaller than those of the well-studied Ni-based noble-metal-free OER catalysts in the literature (Supplementary Table S1). At $\eta$ = 0.35 V, the mass activity and specific activity (based on BET surface area, Supplementary Figure S8) for $\alpha$-Ni(OH)$_2$ catalyst were found to be 150.1 A g$^{-1}$ and 0.26 mA cm$^{-2}$, respectively, outperforming other studied catalysts (Table 1). The intrinsic activities of above catalysts were further estimated by turnover frequency (TOF) assuming every metal atom to be catalytically active (Table 1). It was found that $\alpha$-Ni(OH)$_2$ catalyst exhibits the highest TOF of ~3.61 × 10$^{-2}$ s$^{-1}$ at $\eta$ = 0.35 V, which is ~12, ~3.5, and ~6.8 times higher than that of $\beta$-Ni(OH)$_2$ nanoplates, RuO$_2$, and Pt/C catalysts, respectively, at identical conditions (Table 1). The superior OER activity of $\alpha$-Ni(OH)$_2$ could be attributed to the *in situ* formed $\gamma$-NiOOH phase in that the highly oxidized Ni (average oxidation state of 3.6) in $\gamma$-NiOOH can facilitate the formation of hydroperoxy (OOH) species (key intermediates in the OER) and subsequent conversion to O$_2$.[42,50−52] These results suggest that $\alpha$-Ni(OH)$_2$ hollow spheres could serve as an efficient catalyst to drive water oxidation with high stability.

To gain insight into the excellent cycle performance of highly nanostructured $\alpha$-Ni(OH)$_2$ hollow spheres (Supplementary Figure S6a), we conducted "post-mortem" TEM analysis on the electrode material after 500 cycles. As revealed in Figure 3a and b, the morphology and hollow structure of $\alpha$-Ni(OH)$_2$ are all maintained well, except for the moderate increase in surface roughness. This observation is consistent with a previous report that the conversion between $\alpha$-Ni(OH)$_2$ and $\gamma$-NiOOH can be realized without mechanical deformation and material swelling.[53] In sharp contrast, considerable surface corrosion and particle aggregation are observed for $\beta$-Ni(OH)$_2$ hexagonal nanoplates (Figure 3c,d) and $\beta$-Ni(OH)$_2$ nanoparticles (Figure 3e,f), respectively, after 500 cycles. The poor structural stability and thus deactivation may be ascribed to the Jahn−Teller distortion of the low-spin d$^7$ Ni(III) centers of $\beta$-NiOOH.[42] For RuO$_2$ (~36.2 nm) and Pt/C (~2.8 nm Pt on carbon), such continuous potential cycling causes significant migration, aggregation, and detachment of the nanoparticulate catalysts, leading to the loss of the OER (also ORR) activities (Supplementary Figures S6c,d and S9). The electrochemical impedance spectroscopy (EIS) technique was used to provide further insight into the kinetics of electrode reactions. Before cycling (Figure 3g), the Nyquist plots ($Z_{real}$ vs $-Z_{im}$) of the above $\alpha$- and $\beta$-Ni(OH)$_2$ nanocrystals all consist of a depressed semicircle in the high-frequency region (corresponding to charge transfer resistance, $R_{ct}$) and a quasi-sloping line in the low-frequency region (corresponding to mass transfer resistance). Obviously, the $\alpha$-Ni(OH)$_2$ hollow spheres exhibit $R_{ct}$ (diameter of the semicircle) much lower than that of $\beta$-Ni(OH)$_2$ nanocrystals, suggesting the higher charge transport efficiency of the $\alpha$-Ni(OH)$_2$ electrode. After 500 cycles, a greatly reduced $R_{ct}$ (from ca. 4.1 k$\Omega$ to ca. 15 $\Omega$) was found for $\alpha$-Ni(OH)$_2$ hollow spheres (Figure 3h and inset), indicating the activation and improved kinetics of the reaction upon cycling. Such enhanced kinetics may be ascribed to the formation of the active $\gamma$-NiOOH phase and subsequently increased electron conductivity of the electrode. In contrast, the $R_{ct}$ for $\beta$-Ni(OH)$_2$-based electrodes increases dramatically from

ca. 8.8 kΩ to more than 16 kΩ after cycling (Figure 3h and inset), which could be the result of their seriously damaged structures after 500 electrochemical cycles, agreeing well with the CV results and TEM observations.

We also loaded our $\alpha$-Ni(OH)$_2$ catalyst onto carbon fiber paper (CFP) to assess its durability at a high loading of 5 mg cm$^{-2}$ (Supplementary Figure S10). Chronoamperometry measurement ($j$–$t$) was carried out at a constant, moderate $\eta$ of 0.35 V in 0.1 M KOH. As shown in Figure 4, the current density of the $\alpha$-Ni(OH)$_2$-modified CFP electrode increased gradually until it reached a peak value at ~330 min. This activation process is attributed to the conversion of $\alpha$-Ni(OH)$_2$ to OER active $\gamma$-NiOOH phase,[48,49] agreeing with the CV observation in Figure 2a. Afterward, such current density can be maintained, with little decay, over 1440 min of continuous operation, suggesting the high durability of the $\alpha$-Ni(OH)$_2$ catalyst. By contrast, under the exact same condition, the commercial RuO$_2$ catalyst exhibited a continuous decrease in OER activity because of the well-documented instability of RuO$_2$ material in alkaline electrolytes.[35] In addition, digital photos (inset in Figure 4) taken from the $\alpha$-Ni(OH)$_2$-modified CFP electrode show vigorous effervescence at ~60 min (Supplementary Movie S1), comparing favorably with the O$_2$ bubbles formed on a RuO$_2$-coated electrode. The superior long-term durability of the $\alpha$-Ni(OH)$_2$ catalyst at high loading implies the great possibility of implementing this new catalyst into a realistic oxygen evolution electrode.

## CONCLUSION

In summary, we demonstrate the utilization of $\alpha$-Ni(OH)$_2$ hollow spheres as an economical OER catalyst with remarkable activity and stability. The highly nanostructured $\alpha$-Ni(OH)$_2$ catalyst performs significantly better than $\beta$-Ni(OH)$_2$ to evolve O$_2$ from water. It also shows performance superior to that of the state-of-the-art RuO$_2$ catalyst. Our studies here suggest the promise of designing effective electrocatalysts for water oxidation by using the cheap and easily prepared $\alpha$-Ni(OH)$_2$.

## ASSOCIATED CONTENT

**S** Supporting Information

*iR* correction, BET data, additional TEM images, and additional electrochemical data. This material is available free of charge via the Internet at http://pubs.acs.org.

## AUTHOR INFORMATION

**Corresponding Author**

yanys@udel.edu

**Notes**

The authors declare no competing financial interest.

## ACKNOWLEDGMENTS

## REFERENCES

(1) Cook, T. R.; Dogutan, D. K.; Reece, S. Y.; Surendranath, Y.; Teets, T. S.; Nocera, D. G. *Chem. Rev.* **2010**, *110*, 6474.

(2) Walter, M. G.; Warren, E. L.; McKone, J. R.; Boettcher, S. W.; Mi, Q. X.; Santori, E. A.; Lewis, N. S. *Chem. Rev.* **2010**, *110*, 6446.

(3) Dau, H.; Limberg, C.; Reier, T.; Risch, M.; Roggan, S.; Strasser, P. *ChemCatChem.* **2010**, *2*, 724.

(4) Suntivich, J.; May, K. J.; Gasteiger, H. A.; Goodenough, J. B.; Shao-Horn, Y. *Science* **2011**, *334*, 1383.

(5) Lee, S. W.; Carlton, C.; Risch, M.; Surendranath, Y.; Chen, S.; Furutsuki, S.; Yamada, A.; Nocera, D. G.; Shao-Horn, Y. *J. Am. Chem. Soc.* **2012**, *134*, 16959.

(6) Mirzakulova, E.; Khatmullin, R.; Walpita, J.; Corrigan, T.; Vargas-Barbosa, N. M.; Vyas, S.; Oottikkal, S.; Manzer, S. F.; Hadad, C. M.; Glusac, K. D. *Nat. Chem.* **2010**, *4*, 794.

(7) Chen, S.; Duan, J. J.; Jaroniec, M.; Qiao, S. Z. *Adv. Mater.* **2014**, DOI: 10.1002/adma.201305608.

(8) Rossmeisl, J.; Qu, Z. W.; Zhu, H.; Kroes, G. J.; Norskov, J. K. *J. Electroanal. Chem.* **2007**, *607*, 83.

(9) Lee, Y.; Suntivich, J.; May, K. J.; Perry, E. E.; Shao-Horn, Y. *J. Phys. Chem. Lett.* **2012**, *3*, 399.

(10) Gerken, J. B.; McAlpin, J. G.; Chen, J. Y. C.; Rigsby, M. L.; Casey, W. H.; Britt, R. D.; Stahl, S. S. *J. Am. Chem. Soc.* **2011**, *133*, 14431.

(11) Gorlin, Y.; Jaramillo, T. F. *J. Am. Chem. Soc.* **2010**, *132*, 13612.

(12) Liang, Y. Y.; Li, Y. G.; Wang, H. L.; Zhou, J. G.; Wang, J.; Regier, T.; Dai, H. J. *Nat. Mater.* **2011**, *10*, 780.

(13) Yeo, B. S.; Bell, A. T. *J. Am. Chem. Soc.* **2011**, *133*, 5587.

(14) Robinson, D. M.; Go, Y. B.; Greenblatt, M.; Dismukes, G. C. *J. Am. Chem. Soc.* **2010**, *132*, 11467.

(15) Wee, T. L.; Sherman, B. D.; Gust, D.; Moore, A. L.; Moore, T. A.; Liu, Y.; Scaiano, J. C. *J. Am. Chem. Soc.* **2011**, *133*, 16742.

(16) Trotochaud, L.; Ranney, J. K.; Williams, K. N.; Boettcher, S. W. *J. Am. Chem. Soc.* **2012**, *134*, 17253.

(17) Miller, E. L.; Rocheleau, R. E. *J. Electrochem. Soc.* **1997**, *144*, 1995.

(18) Tilak, B. V.; Lu, P. W. T.; Colman, J. E.; Srinivasan, S. *Comprehensive Treatise of Electrochemistry*; Springer: New York, 1981.

(19) Smith, R. D. L.; Prevot, M. S.; Fagan, R. D.; Zhang, Z. P.; Sedach, P. A.; Siu, M. K. J.; Trudel, S.; Berlinguette, C. P. *Science* **2013**, *340*, 60.

(20) Li, Y. G.; Hasin, P.; Wu, Y. Y. *Adv. Mater.* **2010**, *22*, 1926.

(21) Gardner, G. P.; Go, Y. B.; Robinson, D. M.; Smith, P. F.; Hadermann, J.; Abakumov, A.; Greenblatt, M.; Dismukes, G. C. *Angew. Chem., Int. Ed.* **2012**, *51*, 1616.

(22) Landon, J.; Demeter, E.; Inoglu, N.; Keturakis, C.; Wachs, I. E.; Vasic, R.; Frenkel, A. I.; Kitchin, J. R. *ACS Catal.* **2012**, *2*, 1793.

(23) Gong, M.; Li, Y. G.; Wang, H. L.; Liang, Y. Y.; Wu, J. Z.; Zhou, J. G.; Wang, J.; Regier, T.; Wei, F.; Dai, H. J. *J. Am. Chem. Soc.* **2013**, *135*, 8452.

(24) Chen, S.; Qiao, S. Z. *ACS Nano* **2013**, *7*, 10190.

(25) Chen, S.; Duan, J. J.; Jaroniec, M.; Qiao, S. Z. *Angew. Chem., Int. Ed.* **2013**, *52*, 13567.

(26) Gao, M. R.; Xu, Y. F.; Jiang, J.; Zheng, Y. R.; Yu, S. H. *J. Am. Chem. Soc.* **2012**, *134*, 2930.

(27) Gao, M. R.; Xu, Y. F.; Jiang, J.; Yu, S. H. *Chem. Soc. Rev.* **2013**, *42*, 2986.

(28) Kanan, M. W.; Nocera, D. G. *Science* **2008**, *321*, 1072.

(29) Cobo, S.; Heidkamp, J.; Jacques, P. A.; Fize, J.; Fourmond, V.; Guetaz, L.; Jousselme, B.; Ivanova, V.; Dau, H.; Palacin, S.; Fontecave, M.; Artero, V. *Nat. Mater.* **2012**, *11*, 802.

(30) Dinca, M.; Surendranath, Y.; Nocera, D. G. *Proc. Natl. Acad. Sci. U.S.A.* **2010**, *107*, 10337.

(31) Bockris, J. O.; Otagawa, T. *J. Electrochem. Soc.* **1984**, *131*, 290.

(32) May, K. J.; Carlton, C. E.; Stoerzinger, K. A.; Risch, M.; Suntivich, J.; Lee, Y. L.; Grimaud, A.; Shao-Horn, Y. *J. Phys. Chem. Lett.* **2012**, *3*, 3264.

(33) Yin, Q. S.; Tan, J. M.; Besson, C.; Geletii, Y. V.; Musaev, D. G.; Kuznetsov, A. E.; Luo, Z.; Hardcastle, K. I.; Hill, C. L. *Science* **2010**, *328*, 342.

(34) Artero, V.; Chavarot-Kerlidou, M.; Fontecave, M. *Angew. Chem., Int. Ed.* **2011**, *50*, 7238.

(35) Kinoshita, K. *Electrochemical Oxygen Technology*; Wiley-Interscience: New York, 1992.

(36) Kenney, M. J.; Gong, M.; Li, Y. G.; Wu, J. Z.; Feng, J.; Lanza, M.; Dai, H. J. *Science* **2013**, *342*, 836.

(37) Lyons, M. E. G.; Cakara, A.; O'Brien, P.; Godwin, I.; Doyle, R. L. *Int. J. Electrochem. Soc.* **2012**, *7*, 11768.

(38) Chen, J.; Bradhurst, D. H.; Dou, S. X.; Liu, H. K. *J. Electrochem. Soc.* **1999**, *146*, 3606.

(39) McBreen, J. In *Handbook of Battery Materials*; Besenhard, J. Q., Ed.; Wiley-VCH: Cambridge, U.K., 1999.

(40) Subbaraman, R.; Tripkovic, D.; Strmcnik, D.; Chang, K. C.; Uchimura, M.; Paulikas, A. P.; Stamenkovic, V.; Markovic, N. M. *Science* **2011**, *334*, 1256.

(41) Subbaraman, R.; Tripkovic, D.; Chang, K. C.; Strmcnik, D.; Paulikas, A. P.; Hirunsit, P.; Chan, M.; Greeley, J.; Stamenkovic, V.; Markovic, N. M. *Nat. Mater.* **2012**, *11*, 550.

(42) Bediako, D. K.; Lassalle-Kaiser, B.; Surendranath, Y.; Yano, J.; Yachandra, V. K.; Nocera, D. G. *J. Am. Chem. Soc.* **2012**, *134*, 6801.

(43) Bediako, D. K.; Surendranath, Y.; Nocera, D. G. *J. Am. Chem. Soc.* **2013**, *135*, 3662.

(44) Xu, L. P.; Ding, Y. S.; Chen, C. H.; Zhao, L. L.; Rimkus, C.; Joesten, R.; Suib, S. L. *Chem. Mater.* **2008**, *20*, 308.

(45) Jeevanandam, P.; Koltypin, Y.; Gedanken, A. *Nano Lett.* **2001**, *1*, 263.

(46) Soler-Illia, G. J. d. A. A.; Jobbagy, M.; Regazzoni, A. E.; Blesa, M. A. *Chem. Mater.* **1999**, *11*, 3140.

(47) Yan, J.; Fan, Z. J.; Sun, W.; Wei, T.; Zhang, Q.; Zhang, R. F.; Zhi, L. J.; Wei, F. *Adv. Funct. Mater.* **2012**, *22*, 2632.

(48) Oliva, P.; Leonardi, J.; Laurent, J. F.; Delmas, C.; Braconnier, J. J.; Figlarz, M.; Fievet, F.; Deguibert, A. *J. Power Sources* **1982**, *8*, 229.

(49) Medway, S. L.; Lucas, C. A.; Kowal, A.; Nichols, R. J.; Johnson, D. *J. Electroanal. Chem.* **2006**, *587*, 172.

(50) Juodkazis, K.; Juodkazyte, J.; Vilkauskaite, R.; Jasulaitiene, V. *J. Solid State Electrochem.* **2008**, *12*, 1469.

(51) Singh, A.; Chang, S. L. Y.; Hocking, R. K.; Bach, U.; Spiccia, L. *Energy Environ. Sci.* **2013**, *6*, 579.

(52) Wang, J.; Zhong, H. X.; Qin, Y. L.; Zhang, X. B. *Angew. Chem., Int. Ed.* **2013**, *52*, 5248.

(53) Kamath, P. V.; Dixit, M.; Indira, L.; Shukla, A. K.; Kumar, V. G.; Munichandraiah, N. *J. Electrochem. Soc.* **1994**, *141*, 2956.